

## Comprehensive study of reaction mechanisms for the ${}^9\text{Be} + {}^{144}\text{Sm}$ system at near- and sub-barrier energies

P. R. S. Gomes,<sup>1,\*</sup> I. Padron,<sup>1,2</sup> E. Crema,<sup>3</sup> O. A. Capurro,<sup>4</sup> J. O. Fernández Niello,<sup>4</sup> A. Arazi,<sup>4</sup> G. V. Martí,<sup>4</sup> J. Lubian,<sup>1</sup> M. Trotta,<sup>5</sup> A. J. Pacheco,<sup>4</sup> J. E. Testoni,<sup>4</sup> M. D. Rodríguez,<sup>4</sup> M. E. Ortega,<sup>4</sup> L. C. Chamon,<sup>3</sup> R. M. Anjos,<sup>1</sup> R. Veiga,<sup>1</sup> M. Dasgupta,<sup>6</sup> D. J. Hinde,<sup>6</sup> and K. Hagino<sup>7</sup>

<sup>1</sup>*Instituto de Física, Universidade Federal Fluminense, Avenida Litorânea s/n, Gragoatá, Niterói, RJ 24210-340, Brazil*

<sup>2</sup>*Centro de Aplicaciones Tecnológicas y Desarrollo Nuclear (CEADEN), Playa, Ciudad de la Habana, Cuba*

<sup>3</sup>*Departamento de Física Nuclear, Universidade de São Paulo, Caixa Postal 66318, 05315-970, São Paulo, SP, Brazil*

<sup>4</sup>*Laboratorio Tandem, Departamento de Física, Comisión Nacional de Energía Atómica, Avenida del Libertador 8250 (1429), Buenos Aires, Argentina*

<sup>5</sup>*INFN-Sezione di Napoli, I-80126, Napoli, Italy*

<sup>6</sup>*Department of Nuclear Physics, Research School of Physical Sciences and Engineering, Australian National University, Canberra, ACT 0200, Australia*

<sup>7</sup>*Department of Physics, Tohoku University, Sendai 980-8578, Japan*

(Received 20 February 2006; published 28 June 2006)

The delayed x-ray detection technique was used to measure complete and incomplete fusion cross sections for the  ${}^9\text{Be} + {}^{144}\text{Sm}$  reaction at sub- and near-barrier energies. Elastic and inelastic scattering for this system were also measured. Reaction cross sections were derived and the transfer cross sections of one neutron were calculated. The suppression of complete fusion above the barrier, of the order of 10%, is attributed to  ${}^9\text{Be}$  breakup and is considerably smaller than the value of 30% found for the  ${}^9\text{Be} + {}^{208}\text{Pb}$  system.

DOI: [10.1103/PhysRevC.73.064606](https://doi.org/10.1103/PhysRevC.73.064606)

PACS number(s): 25.70.Jj, 25.70.Mn, 24.10.Eq, 25.60.Gc

### I. INTRODUCTION

Widespread theoretical and experimental efforts have been devoted in recent years to understanding the influence of breakup of weakly bound nuclei on fusion cross sections [1]. There is special interest in this subject, since fusion of very weakly bound and exotic radioactive nuclei are reactions of great astrophysical interest and may also play a role in the formation of new very heavy isotopes in the future. Conflicting predictions have been made about whether the fusion of such nuclei is enhanced or hindered by the strong coupling to the breakup channel at both above- and below-barrier energies [2–7]. It has been suggested [2] that the excitation of the soft dipole resonance of halo nuclei and the very large radii of these nuclei would lead to an increase of the fusion cross section at sub-barrier energies. However, it was later realized that the breakup process produces strong couplings between the elastic channel and the continuum states and can, therefore, inhibit the fusion cross section [3]. Experimentally, the relatively low intensities of radioactive beams presently available make extensive studies difficult. However, measurements with stable weakly bound nuclei, which also have high breakup probability, allow similar studies to be performed with good statistics and precision. The most suitable stable nuclei for such studies are  ${}^9\text{Be}$ ,  ${}^6\text{Li}$ , and  ${}^7\text{Li}$ , which have breakup threshold energies between 1.48 and 2.45 MeV. So, the investigation of the fusion, breakup and elastic scattering processes induced by stable weakly bound nuclei is an important reference to similar studies involving exotic radioactive beams.

Several reaction mechanisms have to be considered, in addition to the usual direct complete fusion (DCF), transfer reactions, and inelastic excitations [represented by P1, P2, and P3 in Fig. 1(a), respectively], when one wants to study the effect of breakup on fusion cross sections. In Fig. 1(b) we show typical reaction mechanisms following the breakup of weakly bound projectiles: noncapture breakup (NCBU-P4), when neither of the breakup fragments is captured by the target; incomplete fusion (ICF-P5), when one of the breakup fragments is captured by the target; and sequential complete fusion (SCF-P6), when breakup occurs followed by the successive capture of all the fragments by the target. In summary, the total breakup cross section is the sum of three contributions: NCBU, ICF, and SCF ( $P4 + P5 + P6$ ); complete fusion (CF) is the sum  $\text{DCF} + \text{SCF}$  ( $P1 + P6$ ), whereas the sum of complete and incomplete fusion ( $P1 + P5 + P6$ ) is called total fusion (TF).

Experimentally, it is impossible to discriminate the direct complete fusion, DCF, from the sequential complete fusion following breakup, SCF, and it is very difficult to separate direct transfer reactions from ICF leading to the same final nucleus. Also, experimentally it is not always easy to separate the CF from the transfer plus ICF ( $P2 + P5$ ) processes. Particularly for reactions with light target nuclei, the evaporation residues following these processes are very similar or identical, and therefore the direct identification of residues cannot be used to distinguish them. This is the reason why most of the available data in the literature correspond to TF cross sections, although the main interest is in the behavior of the CF cross section.

The breakup of  ${}^9\text{Be}$  is even more complex, since fragmentation of  ${}^9\text{Be}$  into  ${}^8\text{Be} + n$  is not the only possible  ${}^9\text{Be}$  breakup mechanism. Here the unstable  ${}^8\text{Be}$ , with a half-life of 0.07 fs, breaks up into two  $\alpha$  particles. However, the  ${}^9\text{Be}$

\*Corresponding author; E-mail: paulogom@if.uff.br

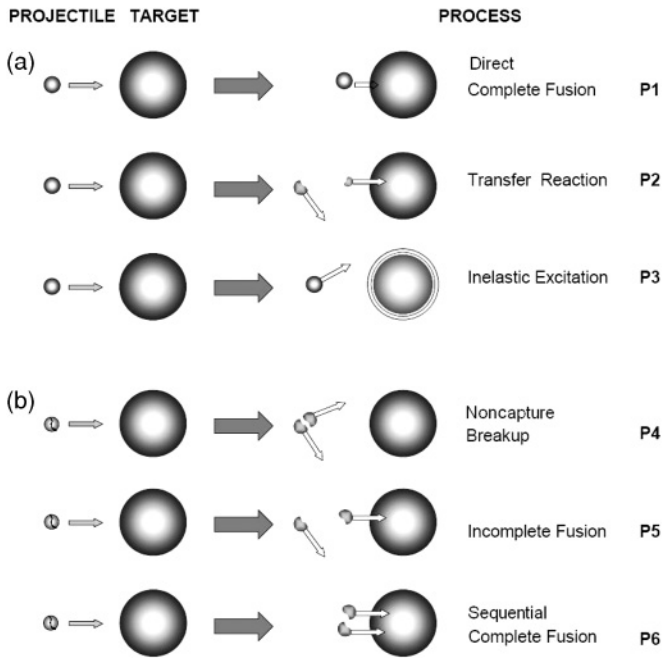


FIG. 1. Schematic diagrams of reaction mechanisms (a) involving any kind of nuclei and (b) involving weakly bound nuclei.

itself may undergo a prompt breakup process  ${}^9\text{Be} \rightarrow \alpha + \alpha + n$  ( $Q = -1.57$  MeV) or  ${}^9\text{Be} \rightarrow \alpha + {}^5\text{He}$  ( $Q = -2.47$  MeV). Therefore, the  ${}^9\text{Be}$  breakup is defined [8] as the excitation of the  ${}^9\text{Be}$  to energies above the dissociation threshold for one or more decay channels, as a result of which it disassociates, ultimately leading to the production of  $\alpha$  particles.

The reaction processes following the  ${}^9\text{Be}$  prompt breakup are shown schematically in Fig. 2. P7 is the prompt noncapture breakup, P8 is the ICF with one  $\alpha$  particle fragment fusing with the target, and P9 is SCF, with all fragments fusing with the target. As a consequence, reactions induced by the  ${}^9\text{Be}$  projectile may lead to the three processes where no breakup is involved (P1 to P3) and to at least six different breakup processes (P4 to P9). The usual measurement of the total fusion cross section involving the  ${}^9\text{Be}$  projectile includes the following processes: P1 ( ${}^9\text{Be} + \text{target}$ ), P2a ( $\alpha + \text{target}$ ), P5 ( ${}^8\text{Be} + \text{target}$ ), P6 ( ${}^9\text{Be} + \text{target}$ ), P8 ( $\alpha + \text{target}$ ), and P9 ( ${}^9\text{Be} + \text{target}$ ). In some experiments [9–12], it was possible to separate the fusion of  $\alpha$  particles from the fusion of  ${}^9\text{Be}$

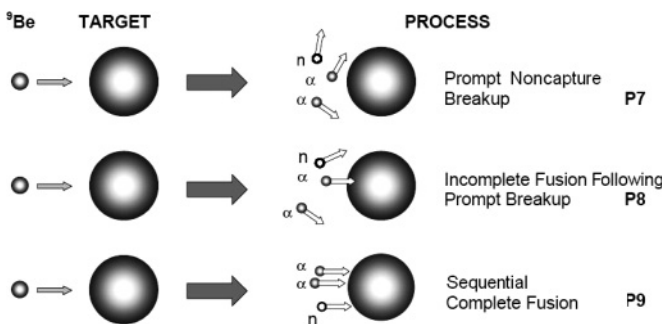


FIG. 2. Schematic diagrams of particular reaction mechanisms involving  ${}^9\text{Be}$  as a projectile.

and  ${}^8\text{Be}$  with the target, and therefore the sum of the cross sections of the processes P1, P5, P6, and P9 were obtained separately from the sum of P2a and P8. When experiments involve the measurement of single  $\alpha$  particles, the yield of  $\alpha$  particles corresponds to the following expression [8]:

$$\sigma_{\alpha \text{ singles}} = \sigma_{\text{ICF}} + 2(\sigma_{1n \text{ transfer}} + \sigma_{\text{NCBU}}), \quad (1)$$

where  $\sigma_{\text{ICF}}$  corresponds to processes P2a + P8,  $\sigma_{1n \text{ transfer}}$  is the one-neutron transfer to the target and the following  ${}^8\text{Be}$  breakup into two  $\alpha$ s (P2b), and  $\sigma_{\text{NCBU}}$  is the sum of the cross sections of process P4 and P7. The yield of two  $\alpha$  particles in coincidence corresponds to

$$\sigma_{\alpha-\alpha \text{ coincidences}} = \sigma_{1n \text{ transfer}} + \sigma_{\text{NCBU}}. \quad (2)$$

Some reactions involving stable weakly bound projectiles and heavy targets produce compound nuclei decaying by  $\alpha$  emission. In those cases, the characteristic energies and half-lives of the emitted  $\alpha$  particles may be used to unambiguously identify the evaporation residues. This technique was used in experiments [8–14] where the fusion of  $\alpha$  particles (ICF) was separated from the fusion of  ${}^9\text{Be}$  and  ${}^8\text{Be}$  (included experimentally in CF), and fusion of a deuteron (triton) was separated from CF when  ${}^6\text{Li}$  ( ${}^7\text{Li}$ ) projectiles were used. Suppressions of CF at energies above the barrier were found to be 20%–30% for  ${}^{208}\text{Pb}$  and  ${}^{209}\text{Bi}$  targets, when compared with the predictions of coupled channels (CC) calculations that do not take into account the breakup process. If the measured ICF cross sections are added to the CF, the derived TF cross sections, at above-barrier energies, correspond closely to the predictions of the CC calculations. In the sub-barrier region, no strong conclusions were drawn from the available data.

The sub-barrier breakup of  ${}^9\text{Be}$  on  ${}^{208}\text{Pb}$  and  ${}^{197}\text{Au}$  was measured by Hinde *et al.* [15], where it was possible to distinguish the prompt breakup (P7) from the long-lived  ${}^8\text{Be}$  ground-state breakup following transfer or Coulomb excitation. The prompt breakup probabilities were found to be large and could qualitatively explain the large suppression of CF at above-barrier energies. It was determined that for the  ${}^9\text{Be} + {}^{208}\text{Pb}$  system at small projectile-target distances, the probability of occurrence of prompt breakup is much larger than for the  $1n$  transfer +  ${}^8\text{Be}_{\text{G.S}}$  or inelastic excitation. Furthermore, it was concluded that only the prompt breakup may affect the CF cross section, since the long half-life of the  ${}^8\text{Be}$  allows it to interact with the target before it breaks up into two  $\alpha$  particles. In this work, it was predicted that the ICF probability for any target scales almost linearly with the charge of the target nucleus. However, these predictions could not be tested so far, since the measurement of fusion cross sections induced by  ${}^9\text{Be}$  on lighter targets either (i) estimate ICF cross sections smaller than 10% for the  ${}^{64}\text{Zn}$  target, which are within the experimental uncertainties [16–18], or (ii) determine TF, as for the  ${}^{27}\text{Al}$  target [19]. Measurements of CF and ICF with targets in the medium-mass range are lacking, inhibiting experimental investigation of how the CF suppression evolves from heavy to light systems.

The coverage of this gap is not an easy task, because when medium-mass targets are used, the evaporation residues do not decay by  $\alpha$  emission. We proposed, as an alternative method, the detection of decay x rays, which can be used when the

residual nuclei decay by electron capture with half-lives from some minutes to many hours, including at least two generations of decay. This method was successfully applied during the 1980s [20–24] in the study of sub-barrier fusion of tightly bound nuclei and recently for the  ${}^6\text{He} + {}^{64}\text{Zn}$  system [25].

Among the systems involving stable weakly bound projectiles and medium-mass target for which this method could be applied,  ${}^9\text{Be} + {}^{144}\text{Sm}$  is suitable, since all the CF evaporation residues decay by electron capture. Their half-lives are compatible with the experimental time scale, and their decay properties allow the measurement of two generations of x-ray emitters. Furthermore, since  ${}^{144}\text{Sm}$  is a spherical nucleus, a comparison with the  ${}^9\text{Be} + {}^{208}\text{Pb}$  reaction is simplified. Predictions of the evaporation code PACE [26] show that, following CF, the compound nucleus  ${}^{153}\text{Dy}$  decays mainly by neutron evaporation in the energy range of interest. Thus CF leads to residues distinct from those produced by the  $\alpha$  ICF. The cross section of an important channel following ICF can also be determined by this method. Figure 3 shows the PACE predictions for the evaporation of the fusion of  ${}^9\text{Be} + {}^{144}\text{Sm}$ , using a level density parameter  $A/8$ . We tested the variation of the predictions for different values of level density parameters, from  $A/11$  to  $A/7$ , and the results are qualitatively very similar.

In this paper we report the measurement of cross sections for CF and ICF for the reaction of  ${}^9\text{Be}$  with a medium-mass target, namely  ${}^9\text{Be} + {}^{144}\text{Sm}$ . This was performed at sub- and near-barrier energies by detecting delayed x rays emitted by the electron capture decay of the CF and ICF evaporation residues. The detection of delayed x rays was complemented by the detection of delayed  $\gamma$  rays emitted by some of the residues. Additionally, by the simultaneous measurement of elastic and inelastic scattering angular distributions for this system, we

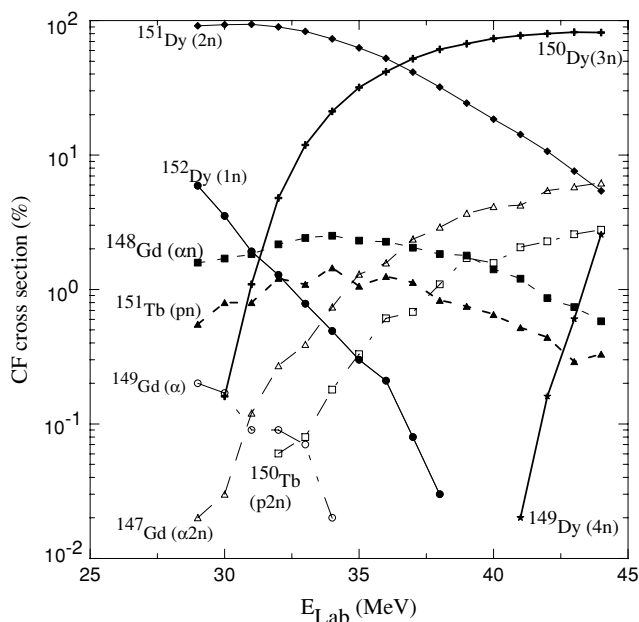


FIG. 3. Predictions of the evaporation code PACE for the evaporation following the complete fusion of  ${}^9\text{Be} + {}^{144}\text{Sm}$ , using level density parameter  $A/8$ .

could also derive reaction and inelastic cross sections. The sum of noncapture breakup and  $1\alpha$ , and  $1n$  transfer cross sections could then be estimated by subtracting total fusion + inelastic cross sections from the total reaction cross section. We also estimated the cross sections for the  $1n$  transfer channel, and therefore we were able to perform a comprehensive study of the reaction mechanisms present when a stable weakly bound projectile is involved. Some of these data have been previously reported [27].

In Sec. II of this paper we present the experimental methods and the characteristics of the decay scheme for CF and ICF evaporation residues. In Sec. III we show the experimental results. In Sec. IV we show the procedures for the derivation of the cross sections. In Sec. V we compare the data with theoretical CC calculations. Finally, in Sec. VI we present a general discussion and conclusions.

## II. EXPERIMENTAL METHODS

The predictions of the evaporation code PACE [26] for the CF of the  ${}^9\text{Be} + {}^{144}\text{Sm}$  system show that the compound nucleus  ${}^{153}\text{Dy}$  decays mainly by neutron evaporation, with  $2n$  ( ${}^{151}\text{Dy}$ ) and  $3n$  ( ${}^{150}\text{Dy}$ ) being dominant in the energy range from 0.8 to 1.4 times the Coulomb barrier, as shown in Fig. 3. Fission decay is not predicted to occur for this reaction in this energy range. It is important to note that, as in previous measurements with  ${}^9\text{Be}$  [9–12], we are unable to separate fusion of  ${}^9\text{Be}$  with the target from fusion of  ${}^8\text{Be}$  with the target, and therefore what we call CF is in fact the sum of CF and any  ${}^8\text{Be} + {}^{144}\text{Sm}$  fusion. The half-lives and decay properties of all evaporation residues are shown in Table I. We should be able to measure all evaporation channels, apart from the  $\alpha n$  ( ${}^{148}\text{Gd}$ ), which has a half-life of 98 y. However, this channel is predicted to be negligible for most of the energy range studied, being calculated to contribute less than 2% of the CF cross section even at the highest energy.

PACE predictions for the products of the ICF channel suffer from not knowing the energy of the captured  $\alpha$  particle originated from the breakup. If we assume, for simplicity, that it is  $(4/9)E({}^9\text{Be}) - S_n$ , where  $S_n$  is the breakup threshold energy of the  ${}^9\text{Be}$ , the predictions are that the main evaporation products are from the  ${}^4\text{He}$  ICF  $1n$  evaporation channel ( ${}^{147}\text{Gd}$  with  $T_{1/2} = 38.1$  h). Other possible channels are  ${}^{148}\text{Gd}$  ( $0n$  channel with  $T_{1/2} = 98$  yr) and  ${}^{146}\text{Gd}$  ( $2n$  channel with  $T_{1/2} = 48.3$  days). These could not be measured owing to their very long half-lives. Consequently, only a lower limit of the ICF cross section can be determined. However, at the highest bombarding energies,  ${}^{147}\text{Gd}$  may also be produced by  $\alpha 2n$  evaporation following complete fusion, as will be discussed later. The nucleus  ${}^{147}\text{Gd}$  could also be produced following direct transfer of one  $\alpha$  to the target. However,  $Q$  value and  $Q_{\text{opt}}$  considerations ( $Q = 4.26$  MeV and  $E_{\text{opt}}^* = 22.26$  MeV at  $E_{\text{Lab}} = 40$  MeV) show that the direct transfer favors highly excited states in  ${}^{148}\text{Gd}$ , much above the particle emission threshold. The most probable decay channel for such excitation energy is the  $2n$  channel. Thus we expect the contribution from transfer to be small, and subsequently we will identify the  ${}^{147}\text{Gd}$  yield with ICF.

TABLE I. Decay properties of the evaporation residues corresponding to the complete fusion of  ${}^9\text{Be} + {}^{144}\text{Sm}$  and the incomplete fusion of  $\alpha + {}^{144}\text{Sm}$ , in the energy range of interest.

	Channel	Nucleus	1 <sup>st</sup> decay generation	2 <sup>nd</sup> decay generation
Complete fusion	1n	${}^{152}\text{Dy}$	2.37 h	17.5 h/4.2 min
	2n	${}^{151}\text{Dy}$	17 min/6% $\alpha({}^{147}\text{Gd})$	17.6 h
	3n	${}^{150}\text{Dy}$	7.17 min/31% $\alpha({}^{146}\text{Gd})$	3.3 h/6.0 min
	4n	${}^{149}\text{Dy}$	4.1 min	4.15 h/4.2 min
	pn	${}^{151}\text{Tb}^a$	17.6 h	
	p2n	${}^{150}\text{Tb}$	3.3 h/6.0 min	
	$\alpha n$	${}^{148}\text{Gd}$	98 years	
	$\alpha 2n$	${}^{147}\text{Gd}$	38.1 h	
Incomplete fusion	0n	${}^{148}\text{Gd}$	98 years	
	1n	${}^{147}\text{Gd}$	38.1 h	
	2n	${}^{146}\text{Gd}$	48.3 days	

<sup>a</sup>This nucleus has an isomeric state of half-life 25 s. It was neglected because it decays almost completely (more than 93%) to the ground state through an isomeric transition.

Figure 4 shows the part of the table of isotopes corresponding to the compound nuclei and evaporation residues of the CF of the  ${}^9\text{Be}$  and the ICF of one  $\alpha$  particle fragment with the  ${}^{144}\text{Sm}$  target. One can see that most of the CF evaporation channels have two measurable generations of decay.

By measuring elastic and inelastic scattering angular distributions for this system, we could also derive reaction and inelastic excitation functions and the sum of NCBU,  $1\alpha$ , transfer, and  $1n$  transfer cross sections.

### III. EXPERIMENTAL SETUPS AND RESULTS

The experiment was performed at the Tandem Laboratory, Buenos Aires.  $\text{BeO}^-$  was used to produce  ${}^9\text{Be}$  beams, at 10 energies from  $E_{\text{Lab}} = 30$  to 44 MeV ( $V_{B\text{Lab}} \sim 33$  MeV). Five 88.6%-enriched  ${}^{144}\text{Sm}$  targets were used, with thicknesses from 170 to 220  $\mu\text{g}/\text{cm}^2$  on carbon backings of 20  $\mu\text{g}/\text{cm}^2$ .

An aluminum catcher foil was placed a few millimeters behind the target. A suitable catcher foil thickness of 1.6  $\text{mg}/\text{cm}^2$  was chosen, such that it should stop the fusion residues but let the elastically scattered beam particles pass through.

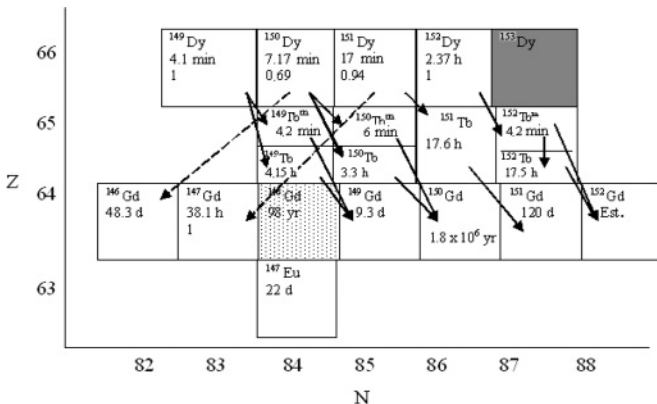


FIG. 4. Decay scheme of the CF and ICF compound nuclei.

One surface-barrier silicon detector was placed at 31.6 degrees to the beam direction, at 24.6 cm from the target, to be used as a monitor for normalization. The solid angle uncertainty was 1.8% and, in the detector angular position, it was 0.1 degrees, leading to an uncertainty of  $\pm 1.3\%$  in the Rutherford cross section. The estimated uncertainty of  $\pm 0.4$  degrees in the beam angle entering the scattering chamber leads to  $\pm 5\%$  uncertainty in the Rutherford cross section. Uncertainty in the beam spot position of  $\pm 1$  mm gives a further  $\pm 2.5\%$  uncertainty in the normalization of the cross sections. Thus, the overall systematic uncertainty in normalization is estimated as  $\pm 6.0\%$ .

To derive reaction and inelastic cross sections, a set of seven surface-barrier detectors was also used to measure (simultaneously with fusion) the elastic and inelastic scattering angular distributions. This set was placed 40 cm from the target, with  $5^\circ$  angular separations between adjacent detectors, and had energy resolutions of the order of 350 keV. In front of each detector a set of collimators and circular apertures were used for definition of the solid angles and to eliminate slit-scattered particles. This experimental array has been previously described in detail elsewhere [16,28]. The relative solid angles of the detectors and the monitor were determined by Rutherford scattering from a thin  ${}^{197}\text{Au}$  target. Although the statistics were quite poor for the inelastic excitations of the first and second excited states of the target [ $E^*(2^+) = 1.66$  MeV and  $E^*(3^-) = 1.81$  MeV], it was possible to derive the sum of their integrated cross sections for most of the bombarding energies, by extrapolating the measured angular distribution range using the predictions of the FRESKO code [29], which was in good agreement with the data in the measured angular range.

The typical irradiation time was 2 h, during which the beam was multiscaled at 1-min intervals. Then both the target and catcher foil were removed and placed in front of the x-ray detector within  $\sim 5$  min. Each catcher foil was used only once. Before a subsequent irradiation using the same target, the residual x-ray counting rate from the previous irradiation was accumulated to subtract the background. After the end of the fusion measurements, extra bombardments were performed

at the same energies to widen the elastic scattering angular distributions.

For the detection of the delayed K x rays, a germanium detector was used, with an energy resolution of 600 eV in the energy range of the the K x rays. The lines to be analyzed were the  $K_{\alpha 1}$  and  $K_{\alpha 2}$  from Tb, Gd, and Eu, from 40.9 to 44.5 keV. The energy separations of the peaks were typically around 700 eV; therefore it was possible to separate the lines. Furthermore, as the relations between the  $K_{\alpha 1}$  and  $K_{\alpha 2}$  lines of each element are well known, they were used to check the consistency of the peak-fit procedure. The peak shape was well determined by the Gd x rays emitted by a standard  $^{152}\text{Eu}$  source. As we needed to separate isotopes with different half-lives producing the same x rays, an automatic set of counting runs was programmed. Because of the half-life characteristics, the following set of counting periods for the delayed x rays was used: three runs of 5 min, three runs of 15 min, and two runs of 30 min each, corresponding to a total counting time of 2 h. For most of the energies, we also accumulated some long runs lasting a few hours.

The energy calibration and detector efficiency were determined by the following standard radioactive sources, with lines in the range from 30 to 300 keV:  $^{152}\text{Eu}$ ,  $^{133}\text{Ba}$ ,  $^{137}\text{Cs}$ ,  $^{241}\text{Am}$ , and  $^{57}\text{Co}$ . The uncertainty in the x-ray yield resulting from uncertainty in the efficiency was calculated to be  $\pm 3\%$ , leading to the overall systematic uncertainty in cross sections of  $\pm 6.7\%$ .

Figure 5 shows typical K x-ray spectra corresponding to the irradiation with a bombarding energy of 44 MeV, obtained

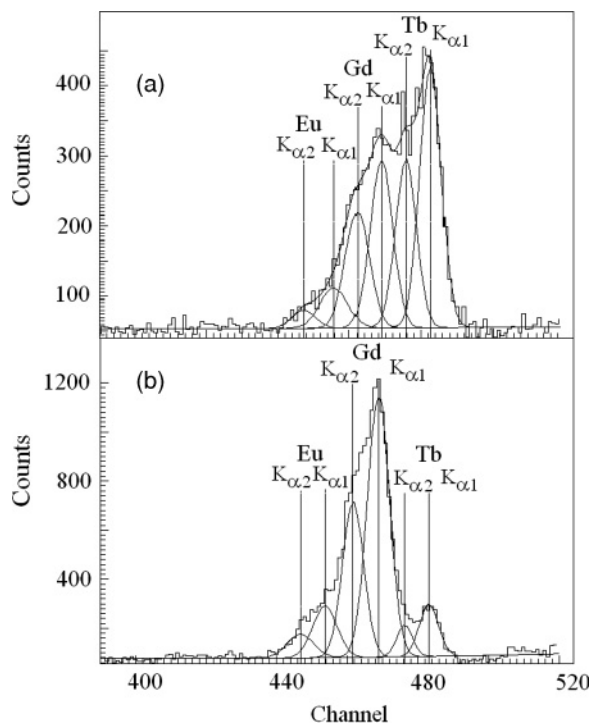


FIG. 5.  $K_{\alpha}$  x-ray spectra taken from (a) 5-mins run taken a few minutes after the end of the irradiation and (b) 30-mins run taken 90 mins after the end of the irradiation.

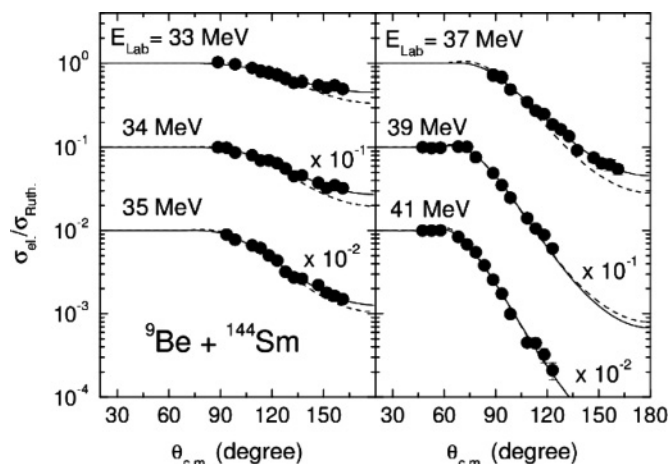


FIG. 6. Elastic scattering angular distributions. The dashed lines correspond to the São Paulo potential predictions without any fit, whereas the full lines correspond to the fits using one normalization factor for the real and one for the imaginary parts of the São Paulo potential. For the highest energies, there was no need to change the standard parameters.

from a 5-min run taken a few minutes after the end of the irradiation, and from a 30-min run taken 90 min after the end of the irradiation. One can observe that the relative intensity of the Tb x rays associated with the first decay generation decreases with time, whereas the opposite happens for the Gd x rays.

Figure 6 shows the measured elastic-scattering angular distributions. The explanation of the full and dashed lines will be given in Sec. V of this paper.

#### IV. DERIVATION OF CROSS SECTIONS

In deriving the fusion cross sections, we used a code specially written for this purpose, named XRWEPC [30], adapted from the original x-ray code [31]. In this code, individual evaporation cross sections are fitted simultaneously. The main principles of the code are described in the following.

The fusion cross section is written as

$$\sigma_{\text{fusion}} = \sum_A P_A, \quad (3)$$

where  $P_A$  are the individual evaporation cross sections. The peak area of the  $K_{\alpha}$  x ray is

$$N_{Z-1}(t_I, t_F) = C \sum_A W_{Z,A} F_{Z,A}(t_I, t_F) P_A, \quad (4)$$

where  $t_I$  and  $t_F$  are the initial and final counting times of the run,  $C$  is the normalization constant, which depends on the Rutherford scattering and the x-ray detector efficiency,  $W_{Z,A}$  is the number of  $K_{\alpha}$  x rays produced for each nucleus ( $Z, A$ ) decay,  $F_{Z,A}(t_I, t_F)$  is the number of decays of the nucleus ( $Z, A$ ) per unit production of the residues of mass  $A$ , which is a function of the time dependence of the beam intensity in the irradiation time interval ( $t_I, t_F$ ) and the half-lives of the residual nuclei. The  $P_A$  values are obtained from simultaneous fits of all points of the yields of  $K_{\alpha}$  x rays as a function of time. This procedure allows testing self-consistency, because

within one chain corresponding to one value of  $A$  there is more than one decay generation. Metastable levels are considered as independent decay elements.

The analysis of the x-ray spectra had shown that the Eu  $K_{\alpha}$  x rays were contaminated by a  $\gamma$  ray. This was concluded for two main reasons: First, the  $K_{\alpha 1}/K_{\alpha 2}$  ratio obtained for the Tb and Gd x rays were in agreement with the well-known values, but the same was not true for the Eu. The second reason is that the half-life of the x-ray emission did not correspond to the 38.1 h of  $^{147}\text{Gd}$ , the almost exclusive origin of the observed Eu x rays (as a result of the very long lifetimes of the neighboring Gd isotopes). The contamination problem could be overcome because  $^{147}\text{Gd}$  emits a  $\gamma$  ray of 229.3 keV that was visible in the spectra, in an energy region with a very low background. The half-life of this line was shown to correspond to that of  $^{147}\text{Gd}$ . Therefore, the cross section for the  $^{147}\text{Gd}$  channel was determined by the off-line  $\gamma$ -ray spectroscopy method [32]. The origin of the contamination was a 40.91-keV  $\gamma$  ray originated from contamination of the Al catcher foil by some element with  $Z$  in the region 26 to 29 (Fe, Ni, or Cu). This line corresponds to a transition from the evaporation residue  $^{62}\text{Zn}$ , with  $T_{1/2} = 9$  h. Two other  $\gamma$ -ray lines, originating from another fusion evaporation channel of  $^9\text{Be}$  with the contaminants, were identified: 67.4 and 283 keV, from  $^{61}\text{Cu}$ , with  $T_{1/2} = 3.4$  h.

As the target was not 100% pure, but only 88.6% enriched, we had to take into account the contribution of the heavier Sm isotopes to the x-ray yield. The target impurities comprised 4%  $^{147}\text{Sm}$ , 2%  $^{152}\text{Sm}$ , and less than 2% for the other Sm isotopes. The code PACE, with a level density parameter  $A/8$ , was used to estimate the main evaporation channels for the fusion with the other Sm isotopes. The main  $xn$  evaporation channels for the impurities decay with half-lives of 6.3, 8.1, and 9.9 h. and also with much longer half-lives. Therefore, we included one evaporation channel with an 8.1-h half-life in the program that derives the cross sections, and the x-ray yields corresponding to this channel were not included in the CF cross section of the  $^9\text{Be} + ^{144}\text{Sm}$  reaction. To test the sensitivity of the derived value of the CF cross section to the half-life of this additional evaporation channel, we varied it within the range  $8 \pm 2$  h. The  $^9\text{Be} + ^{144}\text{Sm}$  CF cross sections were not sensitive to this half-life variation.

As the monitor detector used to normalize the cross sections could not distinguish the elastic-scattering contributions from the  $^{144}\text{Sm}$  and from the heavier impurities, the monitor elastic counts were scaled by 0.886 to obtain the correct CF and ICF cross sections.

The results of the CF evaporation cross sections are shown in Fig. 7 as the ratio  $\sigma_{\text{EVi}}/\sigma_{\text{CF}}$  (in %), where  $\sigma_{\text{EVi}}$  is the cross section of the evaporation channel  $i$ . Here we have considered the  $^{147}\text{Gd}$  residual nucleus as originating only from ICF. Figure 8 shows the fusion excitation function of each evaporation channel; the ICF cross section is also included. One can observe that the  $3n$  channel is the most important in most of the energy range studied, except at sub-barrier energies, where the  $2n$  channel predominates. Table II shows the cross sections for each channel, including those with very small cross sections that were not plotted in Figs. 7 and 8. The experimental results are in agreement with the code PACE for

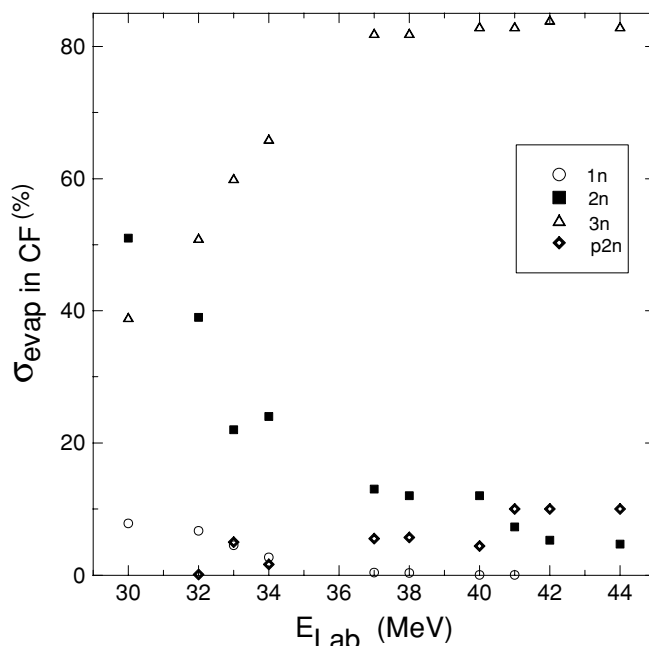


FIG. 7. Ratios for each evaporation channel cross section/CF cross section, as a function of the energy.

the evaporation channels. Fission decay is not predicted to be significant for this system in this energy range.

The reaction cross sections were derived, at each energy, by fitting the elastic angular distributions with an optical model. The uncertainties in these cross sections were derived by allowing variation of the  $\chi^2/N$  (where  $N$  is the number of data points) by one unit. Here, as in the monitor energy spectra, elastic scattering from the isotopic impurities could not be distinguished. The reaction cross sections from each isotope

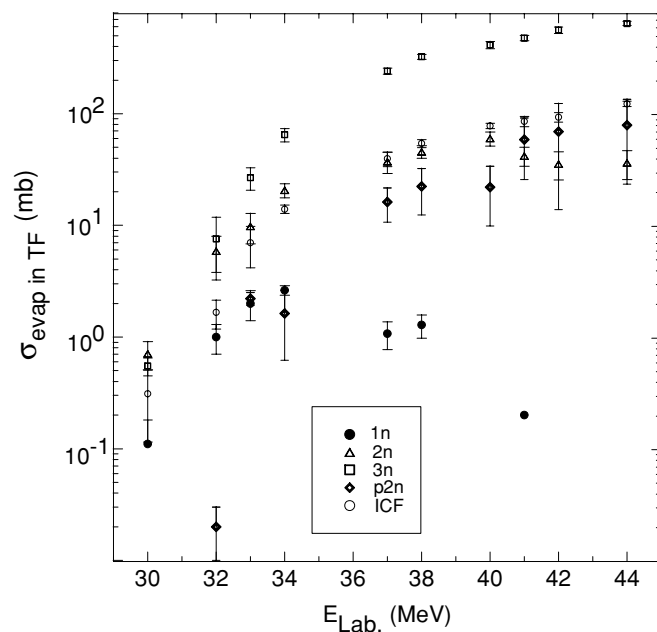


FIG. 8. CF evaporation channels and ICF excitation functions.

TABLE II. Cross sections of each evaporation channel.

$E_{\text{Lab}}$ (MeV)	$^{152}\text{Dy}$ (1n) (mb)	$^{151}\text{Dy}$ (2n) (mb)	$^{151}\text{Tb}$ (pn) (mb)	$^{150}\text{Dy}$ (3n) (mb)	$^{150}\text{Tb}$ (p2n) (mb)	$^{149}\text{Dy}$ (4n) (mb)
30	0.11	0.71	0.01	0.55	—	—
32	1.00	5.84	0.52	7.54	0.02	—
33	2.00	9.82	3.82	26.7	2.21	—
34	2.63	20.6	8.10	64.7	1.62	—
37	1.07	37.1	0.22	241	16.2	—
38	1.28	45.7	1.64	324	22.4	—
40	0.08	59.8	0.11	414	21.9	0.12
41	0.20	41.9	—	476	58.4	0.13
42	—	35.6	2.46	562	68.8	0.43
44	—	36.2	9.80	644	79.0	1.20

are expected to be similar; thus no correction was attempted to account for the isotopic impurities.

Figure 9 and Table III show the measured cross sections obtained in this work: CF, ICF, reaction, and inelastic. Here, no contribution from  $^{147}\text{Gd}$  is considered in CF, giving a lower limit to the CF cross sections at the highest energies. Only an estimate could be derived for ICF since we were unable to measure the  $^{146}\text{Gd}$  and  $^{148}\text{Gd}$  decays. The inelastic scattering cross sections (excitations of the  $^{144}\text{Sm}$ ) have large uncertainties, owing to the poor statistics. The cross sections for the direct reactions (NCBU,  $\alpha$  transfer, and  $1n$  transfer), also shown in Fig. 9 and Table III, were derived from

$$\sigma_{\text{DR}} = \sigma_{\text{NCBU}} + \sigma_{\alpha \text{ transfer}} + \sigma_{1n \text{ transfer}} = \sigma_R - \sigma_{\text{TF}} - \sigma_{\text{Inel}}. \quad (5)$$

A comparison between Eqs. (2) and (5) shows that with the present data and procedure, apart from the  $\alpha$  transfer process, we were able to derive the same quantity as when one performs  $\alpha$ - $\alpha$  coincidence experiments.

In the last column of Table III are shown the experimental ratios  $\sigma(^{147}\text{Gd})/\sigma_{\text{TF}}$ . This can be considered as a model-independent measure of the ratio  $\sigma_{\text{ICF}}/\sigma_{\text{TF}}$ —defined as a suppression factor (SF) for CF—if it is assumed that  $\sigma(^{147}\text{Gd})$  results exclusively from ICF. With this assumption, the ratio corresponds to a lower limit to the suppression factor, since  $\sigma(^{146}\text{Gd})$  and  $\sigma(^{148}\text{Gd})$  could not be measured in this work.

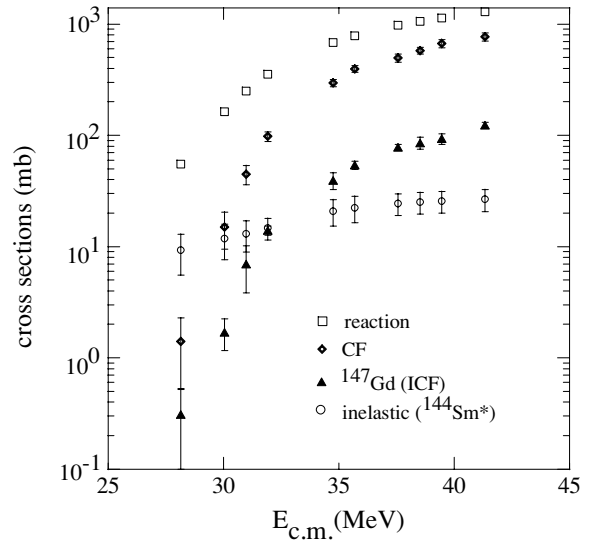


FIG. 9. Measured and derived cross sections obtained in this work: CF, ICF, reaction, inelastic, and DR. See text for details.

The experimental ratio  $\sigma(^{147}\text{Gd})/\sigma_{\text{TF}}$  is shown in Fig. 10, as a function of the energy divided by the average barrier. The average SF is  $13\% \pm 2\%$ , shown by the line in Fig. 10. The contribution to the observed  $^{147}\text{Gd}$  yield from evaporation following CF was estimated using the statistical model code PACE. After this contribution is subtracted, the ratio falls in the range  $13\%$ – $6\%$ , depending on energy. The energy dependence of this ratio may result from our being able to measure only  $\sigma(^{147}\text{Gd})$ —the  $1n$  evaporation channel of the  $\alpha$  ICF. The missing  $\sigma(^{146}\text{Gd})$  may become significant at higher energies, as was observed for the  $^9\text{Be} + ^{208}\text{Pb}$  system at similar relative energies [9,10]. Thus, although  $\sigma(^{147}\text{Gd})$  may not give an absolute value of the SF for the  $^9\text{Be} + ^{144}\text{Sm}$  complete fusion at the higher energies, its value suggests that the SF for this reaction is around  $1/3$  of the one for the reaction  $^9\text{Be} + ^{208}\text{Pb}$  (i.e., of the order of  $10\%$ ).

The results described so far are model independent. In the next section we will compare the data with theoretical calculations.

TABLE III. Measured and derived cross sections.

$E_{\text{c.m.}}$ (MeV)	$\sigma_{\text{CF}}$ (mb)	$\sigma_{\text{ICF}}$ (mb)	$\sigma_{\text{TF}}$ (mb)	$\sigma_{\text{inelastic}}$ ( $2^+ + 3^-$ ) $^{144}\text{Sm}^*$ (mb)	$\sigma_R$ (mb)	$\sigma_{\text{DR}} =$ $\sigma_R - \sigma_{\text{TF}} - \sigma_{\text{inel.}}$ (mb)	$\sigma_{\text{ICF}}/\sigma_{\text{TF}}$ (%)
28.2	$1.41 \pm 0.88$	$0.310 \pm 0.21$	$1.72 \pm 1.02$	$8925 \pm 3.69$	$54.9 \pm 0.5$	$44.0 \pm 3.7$	$18.1 \pm 15.5$
30.1	$14.9 \pm 5.4$	$1.66 \pm 0.54$	$16.6 \pm 6.1$	$11.74 \pm 4.16$	$162.5 \pm 1.5$	$134.2 \pm 7.0$	$10.0 \pm 4.2$
31.1	$44.6 \pm 8.7$	$6.99 \pm 3.17$	$51.6 \pm 10.6$	$12.98 \pm 4.03$	$250.6 \pm 2.2$	$186.0 \pm 11.8$	$13.5 \pm 5.5$
32.0	$97.6 \pm 9.5$	$13.99 \pm 1.3$	$112 \pm 14$	$14.67 \pm 3.25$	$354.4 \pm 3.2$	$227.7 \pm 10.8$	$12.5 \pm 1.7$
34.8	$295 \pm 21$	$39.4 \pm 6.7$	$335 \pm 27$	$20.88 \pm 5.55$	$681.7 \pm 6.1$	$325.8 \pm 26.7$	$11.8 \pm 1.7$
35.8	$395 \pm 27$	$54.1 \pm 4.8$	$449 \pm 24$	$22.35 \pm 5.94$	$784 \pm 7$	$313.1 \pm 31.8$	$12.0 \pm 1.0$
37.5	$496 \pm 42$	$77.8 \pm 4.7$	$574 \pm 42$	$24.37 \pm 5.38$	$971 \pm 9$	$373.5 \pm 46.7$	$13.6 \pm 1.0$
38.6	$577 \pm 39$	$85.4 \pm 10.4$	$663 \pm 40$	$25.06 \pm 5.55$	$1058 \pm 9$	$370.9 \pm 49.4$	$12.9 \pm 1.4$
39.5	$669 \pm 56$	$93.1 \pm 10.0$	$762 \pm 79$	$25.62 \pm 5.68$	$1139 \pm 10$	$352 \pm 65$	$12.2 \pm 1.6$
41.4	$770 \pm 66$	$123 \pm 8$	$893 \pm 79$	$26.52 \pm 5.88$	$1292 \pm 11$	$373 \pm 74$	$13.7 \pm 1.3$

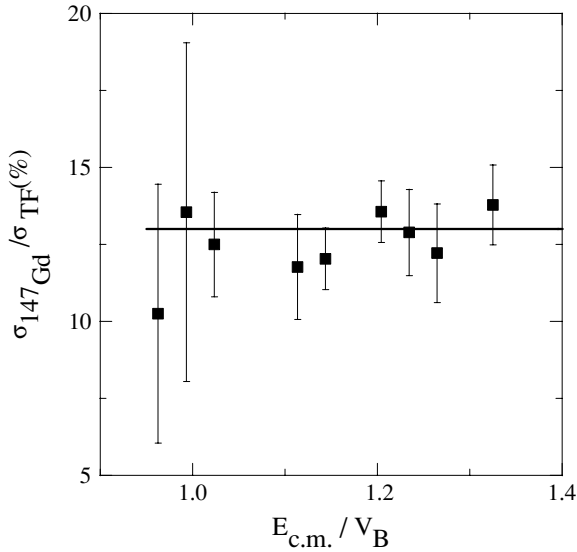


FIG. 10. Ratio of  $\sigma_{\text{ICF}}/\sigma_{\text{TF}}$  as a function of the energy divided by the average barrier energy, assuming that all  $^{147}\text{Gd}$  originate from ICF. The line represents an average suppression factor.

## V. COMPARISON OF THE DATA WITH THEORY

A critical point when one wants to compare the fusion data with theory is the choice of the potential to be used. Depending on the potential characteristics, the conclusions concerning the effect of the breakup on the fusion cross section may be rather different. It is very useful to determine experimentally the fusion barrier distributions (BD), which acts as a strong constraint to the potential parameters, since the potential and couplings used should reproduce the average barrier energy and the shape of the BD obtained experimentally. When the BD is not available, as in the present and many other works, a “reasonable” potential is used, which however might not be appropriate.

We adopted the São Paulo potential (SPP) [33,34] in our present calculations. This potential is based on a double-folding potential and on the Pauli nonlocality involving the exchange of nucleons between projectile and target. It is important to point out that there is no free parameter in this potential. Using the SPP as a global potential requires reliable densities of the nuclei involved. The systematics of nuclear densities has already been established [35,36], including that of  $^9\text{Be}$ . For calculations for elastic scattering, we introduce an imaginary part to the potential, whose geometry we set to be the same as the real part. The default value of the strength is  $\text{Im}[V_{\text{SPP}}] = 0.8 \text{ Re}[V_{\text{SPP}}]$ .

At energies very close to the Coulomb barrier, where coupling effects are important, one needs to use two fit parameters in the SPP, namely the normalization of both the real and imaginary parts of the potential. This was done in fitting the elastic-scattering angular distributions obtained in the present work. In Fig. 6, the dashed lines correspond to the SPP predictions without any adjustment, whereas the full lines correspond to the fits using one normalization factor for the real and one for the imaginary parts of the SPP. For the

highest energies, there was no need to change the standard parameters.

The SPP has been successfully used to describe several reaction mechanisms for a large number of systems in a wide energy range, including fusion excitation functions of tightly bound nuclei, without any parameter-fit procedure [34,37–40].

The consistency of the SPP predictions with the ones of other potentials derived in previous works, for systems including weakly bound nuclei, where experimental barrier distributions were derived, was clearly demonstrated in a recent paper [41]. The results were impressive, since the SPP was able to reproduce total fusion excitation functions, barrier distributions, and CF suppression (for weakly bound projectiles) obtained previously for the  $^9\text{Be} + ^{208}\text{Pb}$  [9,10],  $^{6,7}\text{Li} + ^{209}\text{Bi}$  [10,13], and  $^{16}\text{O} + ^{144}\text{Sm}$  [42] systems. These calculations use an equivalent local Woods-Saxon (WS) potential, that provides similar strengths at the surface region as those from the realistic SPP. For the  $^9\text{Be} + ^{144}\text{Sm}$  system, the WS potential equivalent to the SPP has the following parameters:  $V_o = 140$  MeV,  $r_o = 1.06$  fm, and  $a = 0.71$  fm.

The most appropriate method to calculate fusion of weakly bound nuclei is through continuum-discretized coupled-channels (CDCC) calculations [7]. This method has been applied recently for reactions induced by  $^9\text{Be}$  by considering only three-body breakup ( $^5\text{He} + ^4\text{He}$  or  $^8\text{Be} + n$ ) plus target [43,44], but this is not the most appropriate way to deal with  $^9\text{Be}$  breakup, since the prompt breakup into  $\alpha + \alpha + n$  should be considered. Only recently has this method been developed [45] to deal with four-body reactions (target + three projectile fragments) but its application is not yet available to us. So, we performed CC calculations that do not take into account the effect of breakup (i.e., there is no flux removed through the breakup channel). In this way, we could infer the effect of the breakup on complete fusion by the difference between the results of the calculations and the data. Two codes were used for CC calculations, FRESKO [29] and CCFULL [46], both giving the same results.

We would like to point out that if one wants to include in the coupling scheme the  $^9\text{Be}$  nucleus, which has a large deformation and ground-state rotational band built on a  $K_\pi = 3/2^-$  state, one needs to use a special version of the CCFULL code that incorporates a finite ground-state spin in it, or a special option available in the FRESKO code, to include high-order couplings. The standard derivative form of the coupling interaction potential in the FRESKO code cannot be used when a large deformation is present, since it is valid up to first order in the deformation parameter. The characteristics of  $^9\text{Be}$ , with ground-state spin  $3/2^-$  and consequently a nonzero quadrupole moment in the ground state, gives an additional contribution to the potential in the entrance channel:

$$V(r) = V_o(r) - \langle IM|Y_{20}|IM\rangle\beta_2 R_p dV_o/dr + \dots \quad (6)$$

Here,  $I = 3/2$  is the ground-state spin of  $^9\text{Be}$ , and  $M = \pm 3/2$  or  $1/2$  is the projection of the spin onto the  $z$  axis, which is preserved in the isocentrifugal approximation. The total cross section is given as an average of the contribution from  $M = \pm 3/2$  and  $\pm 1/2$  configurations. In the actual calculation,

we include the highest orders of the expansion in Eq. (6) using the CCFULL scheme. A similar reorientation effect on the potential in the entrance channel has been considered in Ref. [47] for the  ${}^6,7\text{Li} + {}^{59}\text{Co}$  reactions.

As a consequence, when this coupling is considered, the results of the calculations for the fusion cross sections are enhanced at energies above the barrier, which is the opposite behavior to that found with usual couplings. Moreover, the barrier position and height may be changed and the optical potential parameters must be varied to fit the experimental height and radius of the fusion barrier.

For the couplings to  ${}^{144}\text{Sm}$  vibrational excited states, we have used tabulated values:  $\beta_2 = 0.0881$ ,  $r_o = 1.06$  fm, and  $\lambda = 2$  for  $E^* = 1.66$  MeV and  $\beta_3 = 0.14$ ,  $r_o = 1.06$  fm, and  $\lambda = 3$  for  $E^* = 1.81$  MeV. For  ${}^9\text{Be}$ , which has no bound excited state, we considered resonance states in the continuum at  $E^* = 2.43$  and 6.81 MeV, corresponding to states  $5/2^-$  and  $7/2^-$ , respectively, of the  $K = 3/2^-$  ground-state rotational band. Although the excited states in this band are unbound and have a finite width, we can approximately treat them as bound states for the following reasons: The first excited state ( $5/2^-$ ) has a very small width of 0.77 keV; thus the effect of the width is negligible. Moreover, although the second excited state ( $7/2^-$ ) has a large width (1.2 MeV), the excitation energy of this state is quite large (6.8 MeV), and it does not significantly affect the fusion cross sections. Therefore, conclusions from the present calculations remain the same even if we explicitly take into account the width of the excited states. The same effective value of  $\beta_2 = 0.924$  as used in the  ${}^9\text{Be} + {}^{208}\text{Pb}$  reaction [9,10] was adopted. Additionally, the  $1n$  transfer channel with  $Q = -1.48$  MeV was included in the CC calculations performed by the code FRESKO. Transfer to the ground state and the first excited states of  ${}^{145}\text{Sm}$  were included in the calculations, by assuming a spectroscopic factor of 1. The results show a negligible influence of this channel on the fusion cross section.

Figure 11 shows the measurements compared with the CC calculations. The open circles correspond to CF cross sections when no contribution from  ${}^{147}\text{Gd}$  is considered, giving a lower limit of CF. The full circles correspond to the inclusion of the  ${}^{147}\text{Gd}$  cross section and consequently represent lower limits of the TF cross sections (since yields of  ${}^{148}\text{Gd}$  and  ${}^{146}\text{Gd}$  could not be measured). The potential depth was adjusted to match the experimental fusion barrier,  $V_B = 31.2 \pm 0.3$  MeV. The calculation reproduces well the measured TF cross sections above the barrier. Multiplying the calculation by 0.90 gives the best fit to the CF data above the barrier. The CF suppression of  $10\% \pm 3\%$ , shown by a full line in Fig. 11, is compatible with the ratio ICF/TF of the order of 13% determined earlier. The present results, both from analysis of the ICF yield and the comparison of CF with calculation, show a smaller CF suppression than the 24% predicted from Ref. [15], which takes as a reference the 32% measured CF suppression for the  ${}^{208}\text{Pb}$  target [9,10]. For comparison, we mention the results obtained using the SPP and the same method for the CC calculations for the  ${}^9\text{Be} + {}^{208}\text{Pb}$  system [41]. Details of the coupling scheme can be found in Ref. [41]. The fusion data above and below the barrier can be reproduced by the calculations if the predictions are multiplied by a factor

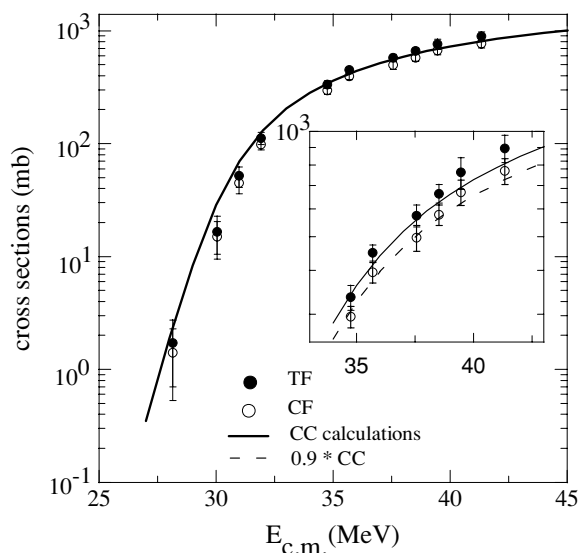


FIG. 11. Experimental lower limits of CF and TF cross sections (open points and full points, respectively) and CC calculation results when excited states of Sm, the Be ground-state rotational band couplings, and  $1n$  transfer are included. The CF suppression at energies above the barrier is derived to be 10%.

of 0.73, corresponding to a 27% CF suppression, much larger than for the  ${}^{144}\text{Sm}$  target.

At sub-barrier energies it is difficult to draw definite conclusions, because theoretical fusion cross sections in this energy region are very sensitive to small modifications in the CC channel calculations. From the calculations performed, small suppression of CF is obtained, relative to the calculations, as can be seen from Fig. 11.

To estimate the  $\text{NCBU} + \alpha$  transfer yields, we have performed CC calculations using the FRESKO code to estimate the  $1n$  transfer cross sections. This reaction channel was not measured nor could it be separated from the NCBU process when we derived the direct reaction cross section. The  $1n$  stripping reaction has a  $Q$  value equal to  $-1.48$  MeV. We have considered in the calculations the ground and the first excited states of  ${}^{145}\text{Sm}$  and we assumed the value for the spectroscopic factor as equal to unity for the transition to both final  ${}^{145}\text{Sm}$  states. In the finite-range transfer calculation, the prior interaction was used, and the standard Wood-Saxon parameters of the  ${}^8\text{Be} + n$  and  ${}^{144}\text{Sm} + n$  interactions were varied to obtain the experimental separation energies. The results are shown in Fig. 12. One can observe that the estimated cross section for this channel is much smaller than the CF. This means that the measured CF, which is actually the sum of the fusion of  ${}^9\text{Be} + {}^{144}\text{Sm}$  with the fusion of  ${}^8\text{Be} + {}^{145}\text{Sm}$  following the  $1n$  transfer, is roughly the same as the first term of this sum.

Figure 13 shows the ratio of yields for different reaction mechanisms to the reaction cross section, as a function of  $E_{c.m.}/V_B$ . The derived  $\sigma_{\text{NCBU}+\alpha \text{ transfer}}$ , is obtained by subtracting from  $\sigma_R$  the measured  $\sigma_{\text{TF}} + \sigma_{\text{inelastic}}$  and the calculated  $\sigma_{1n \text{ transfer}}$ . One can observe that  $\sigma_{\text{NCBU}+\alpha \text{ transfer}}$  is much larger than  $\sigma_{\text{TF}} + \sigma_{\text{inelastic}}$  at the barrier and below

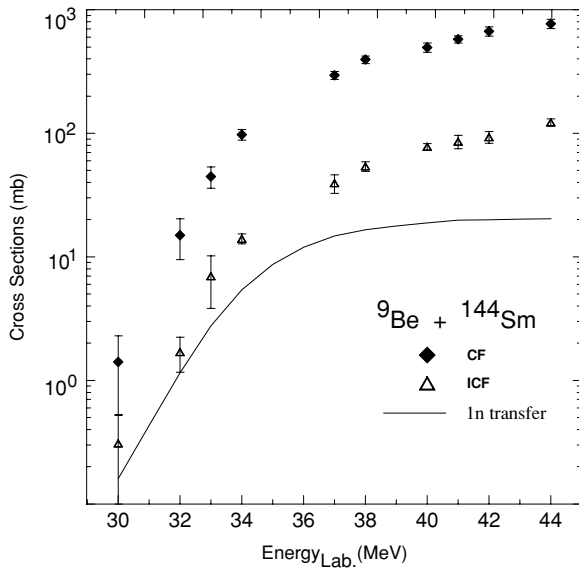


FIG. 12. Calculated  $1n$  transfer cross section for the  ${}^9\text{Be} + {}^{144}\text{Sm}$  system and, for comparison, the measured CF and ICF cross sections.

it, and it corresponds to most of the large reaction cross section (around 80% at  $E = 0.9V_B$ ). The target inelastic excitation is also important at low energies (around 17% at  $E = 0.9V_B$ ). As the energy increases, the relative importance of the fusion processes increases and becomes equal to  $\sigma_{\text{NCBU}} + \sigma_{\alpha \text{ transfer}} + \sigma_{1n \text{ transfer}}$  at  $E \sim 1.1V_B$ . At the highest energy,  $\sigma_{\text{TF}}$  corresponds to 76% of  $\sigma_{\text{R}}$ , compatible with the systematics obtained by Gasques *et al.* [39] for hundreds of systems at this energy region, where an average value of 74% was derived.

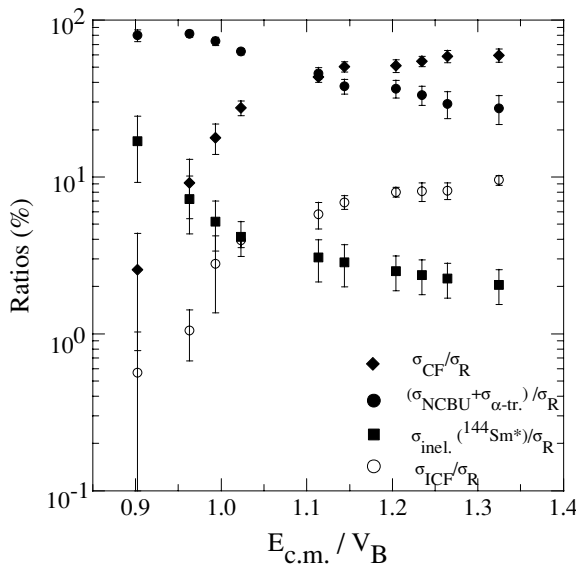


FIG. 13. Ratios between the individual cross sections and the reaction cross section as a function of reduced energy. The derived  $\sigma_{\text{NCBU} + \alpha \text{ transfer}}$  is obtained by subtracting from  $\sigma_{\text{R}}$  the measured  $\sigma_{\text{TF}}$  +  $\sigma_{\text{inelastic}}({}^{144}\text{Sm}^*)$  + calculated  $\sigma_{1n \text{ transfer}}$ .

## VI. SUMMARY AND CONCLUSION

We measured CF cross sections (corresponding to the sum of processes P1 + P5 + P6 + P9), the lower limit of ICF (P8), and the inelastic excitations of the target (P3). We have also performed calculations of the cross section for the  $1n$  transfer (P2b), using the FRESKO code. We also measured the reaction cross section, corresponding to the sum of these 10 processes. We did not measure or calculate the NCBU corresponding to P4 + P7, nor the  $\alpha$  transfer (P2a), but from the measured quantities we were able to estimate  $\sigma_{\text{NCBU}} + \sigma_{\alpha \text{ transfer}}$ . Therefore, a comprehensive analysis of the reaction processes involved was made, contributing to the effort to obtain a systematic description of reaction mechanisms involving weakly bound systems.

As the experimental  $\sigma_{\text{CF}}$  are smaller than those predicted by CC calculations that do not take into account the  ${}^9\text{Be}$  breakup, one can infer that the  ${}^9\text{Be}$  breakup process suppresses CF in the whole energy range studied, both below and above the barrier. In the energy region above the Coulomb barrier, a good fit is obtained if one scales the theoretical results by a factor around 0.90, corresponding to an effective CF suppression of the order of 10%, attributed to the ICF process resulting from prompt  ${}^9\text{Be}$  breakup. This value is smaller than those expected from the suppression determined for heavier targets. So, surprisingly, we found that CF cross sections are only slightly suppressed because of the breakup process, the value of 10% being much smaller than previously reported for reactions with heavier targets. Further detailed study is needed to understand the possible observed change in the effect of breakup on fusion from the Pb/Bi region to Sm.

At sub-barrier energies there is some indication that a small suppression of  $\sigma_{\text{CF}}$  exists, when compared with CC calculations. In this energy regime, contrary to what happens at energies above the barrier, the ICF of one  $\alpha$  particle is not favored, as a simple energy share between the breakup fragments can show that the  $\alpha$  particle would have to tunnel through a relatively higher barrier. Therefore, the main breakup process responsible for an eventual fusion hindrance at sub-barrier energies is the prompt noncapture breakup (P7) associated with low partial waves, since only those partial waves compete with fusion. However, as the results of CC calculations at sub-barrier energies depend strongly on the coupling schemes and potential parameters used, it is hard to draw any strong conclusion concerning the behavior of  $\sigma_{\text{CF}}$  at sub-barrier energies at the moment.

As expected from previous work, noncapture breakup is observed to be the main reaction mechanism at sub-barrier energies, whereas complete fusion predominates at higher energies. The total fusion (CF + ICF) cross sections appear not to be significantly affected by breakup at energies above the barrier. In a naïve picture, we might say that the NCBU associated with low angular momenta removes some flux from fusion. This process is much less significant than ICF at high energies, but it is much more important than ICF at the barrier and below it, and therefore is the main mechanism responsible for the CF suppression at low energies, if it exists. In contrast, the NCBU associated with high angular momenta does not compete with fusion.

Although the present study is an important contribution to the understanding of the effect of breakup on fusion of systems involving weakly bound nuclei, one has to be careful before extending the present conclusions to systems involving other weakly bound nuclei, especially radioactive halo nuclei that have some characteristics not present in  $^9\text{Be}$ .

#### ACKNOWLEDGMENTS

The Brazilian authors would like to thank the CNPq, CAPES, FAPERJ, and FAPESP for their financial support. JOFN, JET, and AJP are members of CONICET. MD and DJH acknowledge support from an ARC Discovery grant.

- 
- [1] L. F. Canto, P. R. S. Gomes, R. Donangelo, and M. S. Hussein, *Phys. Rep.* **424**, 1 (2006).
- [2] N. Takigawa and H. Sagawa, *Phys. Lett.* **B265**, 23 (1991).
- [3] M. S. Hussein, M. P. Pato, L. F. Canto, and R. Donangelo, *Phys. Rev. C* **46**, 377 (1992).
- [4] C. H. Dasso and A. Vitturi, *Phys. Rev. C* **50**, R12 (1994).
- [5] L. F. Canto, R. Donangelo, P. Lotti, and M. S. Hussein, *Phys. Rev. C* **52**, R2848 (1995).
- [6] K. Hagino, A. Vitturi, C. H. Dasso, and S. M. Lenzi, *Phys. Rev. C* **61**, 037602(R) (2000).
- [7] A. Diaz-Torrez and I. J. Thompson, *Phys. Rev. C* **65**, 024606 (2002).
- [8] R. J. Woolliscroft, N. M. Clarke, B. R. Fulton, M. Dasgupta, D. J. Hinde, C. R. Morton, and A. C. Berriman, *Phys. Rev. C* **68**, 014611 (2003).
- [9] M. Dasgupta *et al.*, *Phys. Rev. Lett.* **82**, 1395 (1999).
- [10] M. Dasgupta *et al.*, *Phys. Rev. C* **70**, 024606 (2004).
- [11] C. Signorini *et al.*, *Eur. Phys. J. A* **2**, 227 (1998).
- [12] C. Signorini *et al.*, *Eur. Phys. J. A* **3**, 7 (1999).
- [13] M. Dasgupta *et al.*, *Phys. Rev. C* **66**, 041602(R) (2002).
- [14] Y. W. Wu, Z. H. Liu, C. J. Lin, H. Q. Zhang, M. Ruan, F. Yang, Z. C. Li, M. Trotta, and K. Hagino, *Phys. Rev. C* **68**, 044605 (2003).
- [15] D. J. Hinde, M. Dasgupta, B. R. Fulton, C. R. Morton, R. J. Woolliscroft, A. C. Berriman, and K. Hagino, *Phys. Rev. Lett.* **89**, 272701 (2002).
- [16] S. B. Moraes, P. R. S. Gomes, J. Lubian, J. J. S. Alves, R. M. Anjos, M. M. Sant anna, I. Padr on, and C. Muri, *Phys. Rev. C* **61**, 064608 (2000).
- [17] P. R. S. Gomes *et al.*, *Phys. Rev. C* **71**, 034608 (2005).
- [18] P. R. S. Gomes *et al.*, *Phys. Lett.* **B601**, 20 (2004).
- [19] G. V. Marti *et al.*, *Phys. Rev. C* **71**, 027602 (2005).
- [20] D. E. di Gregorio *et al.*, *Phys. Lett.* **B176**, 322 (1986).
- [21] D. E. di Gregorio *et al.*, *Phys. Rev. C* **39**, 516 (1989).
- [22] S. Gil *et al.*, *Phys. Rev. Lett.* **65**, 3100 (1990).
- [23] M. di Tada *et al.*, *Phys. Rev. C* **47**, 2970 (1993).
- [24] P. R. S. Gomes *et al.*, *Phys. Rev. C* **49**, 245 (1994).
- [25] A. di Pietro *et al.*, *Phys. Rev. C* **69**, 044613 (2004).
- [26] A. Gavron, *Phys. Rev. C* **21**, 230 (1980).
- [27] P. R. S. Gomes *et al.*, *Phys. Lett.* **B634**, 356 (2006).
- [28] A. M. M. Maciel *et al.*, *Phys. Rev. C* **59**, 2103 (1999).
- [29] I. J. Thompson, *Comput. Phys. Rep.* **7**, 167 (1988).
- [30] O. A. Capurro (private communication).
- [31] A. J. Pacheco, D. di Gregorio, J. O. F. Niello, and M. Elgue, *Comput. Phys. Commun.* **52**, 93 (1988).
- [32] P. R. S. Gomes, T. J. P. Penna, R. Liguori Neto, J. C. Acquadro, C. Tenreiro, E. Crema, N. Carlin Filho, and M. M. Coimbra, *Nucl. Instrum. Methods Phys. Res. A* **280**, 395 (1989).
- [33] L. C. Chamon, B. V. Carlson, L. R. Gasques, D. Pereira, C. De Conti, M. A. G. Alvarez, M. S. Hussein, M. A. C andido Ribeiro, E. S. Rossi Jr., and C. P. Silva, *Phys. Rev. C* **66**, 014610 (2002).
- [34] M. A. G. Alvarez, L. C. Chamon, M. S. Hussein, D. Pereira, L. R. Gasques, E. S. Rossi Jr., and C. P. Silva, *Nucl. Phys.* **A723**, 93 (2003).
- [35] C. P. Silva *et al.*, *Nucl. Phys.* **A679**, 287 (2001).
- [36] M. A. G. Alvarez *et al.*, *Phys. Rev. C* **65**, 014602 (2001).
- [37] J. J. S. Alves *et al.*, *Nucl. Phys.* **A748**, 59 (2005).
- [38] J. J. S. Alves *et al.*, *Braz. J. Phys.* **35**, 909 (2005).
- [39] L. R. Gasques, L. C. Chamon, P. R. S. Gomes, and J. Lubian, *Nucl. Phys.* **A764**, 135 (2006).
- [40] D. Pereira, C. P. Silva, L. C. Chamon, J. Lubian, and E. S. Rossi Jr., *Phys. Rev. C* **73**, 014601 (2006).
- [41] E. Crema, L. C. Chamon, and P. R. S. Gomes, *Phys. Rev. C* **72**, 034610 (2005).
- [42] J. R. Leigh, M. Dasgupta, D. J. Hinde, J. C. Mein, C. R. Morton, R. C. Lemmon, J. P. Lestone, J. O. Newton, H. Timmers, and J. X. Wei, *Phys. Rev. C* **52**, 3151 (1995).
- [43] C. Signorini *et al.*, *Nucl. Phys.* **A735**, 329 (2004).
- [44] N. Keeley, N. Alamanos, K. Rusek, and K. W. Kemper, *Phys. Rev. C* **71**, 014611 (2005).
- [45] T. Matsumoto, E. Hiyama, K. Ogata, Y. Iseri, M. Kamimura, S. Chiba, and M. Yahiro, *Phys. Rev. C* **70**, 061601(R) (2004).
- [46] K. Hagino, N. Rowley, and A. T. Kruppa, *Comput. Phys. Commun.* **123**, 143 (1999).
- [47] C. Beck *et al.*, *Phys. Rev. C* **67**, 054602 (2003).